# Exploiting differential effects of actomyosin contractility to control cell sorting among breast cancer cells

Alexander J. Devanny, Michelle B. Vancura, and Laura J. Kaufman*
Department of Chemistry, Columbia University, New York, NY 10027

**ABSTRACT** **In order to gain a greater understanding of the factors that drive spatial organization in multicellular aggregates of cancer cells, we investigate the segregation patterns of 6 breast cell lines of varying degree of mesenchymal character during formation of mixed aggregates. Cell sorting is considered in the context of available adhesion proteins and cellular contractility. It is found that the primary compaction mediator (cadherins or integrins) for a given cell type in isolation plays an important role in compaction speed, which in turn is the major factor dictating preference for interior or exterior position within mixed aggregates. In particular, cadherin-deficient, invasion-competent cells tend to position towards the outside of aggregates, facilitating access to extracellular matrix. Reducing actomyosin contractility is found to have a differential effect on spheroid formation depending on compaction mechanism. Inhibition of contractility has a significant stabilizing effect on cell-cell adhesions in integrin-driven aggregation and a mildly destabilizing effect in cadherin-based aggregation. This differential response is exploited to statically control aggregate organization and dynamically rearrange cells in pre-formed aggregates. Sequestration of invasive cells in the interior of spheroids provides a physical barrier that reduces invasion in three-dimensional culture, revealing a potential strategy for containment of invasive cell types.**

**Monitoring Editor**
Alex Dunn
Stanford University

Received: Jul 15, 2021
Accepted: Aug 17, 2021

## INTRODUCTION

Cell segregation and compartmentalization are important phenomena critical for normal development and cellular function (Garcia-Bellido *et al.*, 1973; Dahmann *et al.*, 2011; Cochet-Escartin *et al.*, 2017). These processes have been studied by biologists and physicists alike, with a particular focus on model systems. In these systems, the differential adhesion hypothesis, first proposed by Steinberg, has been employed to explain sorting (Steinberg, 1962, 1963). This hypothesis proposes that cells destined for different tissues behave as immiscible Newtonian fluids, explore the energy landscape, and reach a minimum energy configuration. Each tissue has a characteristic tissue surface tension, and tissues with higher surface tension are enveloped by those with lower surface tension (Foty *et al.*, 1996). Evidence supporting the differential adhesion hypothesis has been observed in a wide array of biological systems (Technau and Holstein, 1992; Beysens *et al.*, 2000; Foty and Steinberg, 2005; Bécam and Huynh, 2007).

While the tenets of the differential adhesion hypothesis and concept of tissue surface tension have long been viewed as useful principles in cellular organization, their molecular bases have been debated. It was first suggested that observed sorting was due to differences in cell adhesion proteins, namely cadherins. Greater density of available cadherins results in a higher tissue surface tension and more "adhesive" tissue (Steinberg, 2007). Later formulations of this theory suggested that actomyosin contractility should also be considered as a driver of the development of tissue surface tension (Harris, 1976; Krieg *et al.*, 2008). Experimental evidence showing that cells with high cortical tension tended to be enveloped by those with lower cortical tension supported the notion that

This article was published online ahead of print in MBoC in Press (http://www.molbiolcell.org/cgi/doi/10.1091/mbc.E21-07-0357) on August 25, 2021.

Author contributions: A.J.D. and L.J.K. conceived the project and designed the experiments. A.J.D. conducted all experiments and developed data analysis protocols. A.J.D. and M.B.V. performed quantitative data analysis. A.J.D. and L.J.K. prepared the manuscript.

*Address correspondence to: Laura Kaufman (kaufman@chem.columbia.edu).

Abbreviations used: BME, basement membrane extract; ECM, extracellular matrix; EMT, epithelial-to-mesenchymal transition; siRNA, small interfering RNA; 3D, three dimensional.

differential cortex tension alone could drive sorting (Krieg *et al.*, 2008). A more modern view of the differential adhesion hypothesis takes an integrated and dynamic view of the roles of cell adhesion and cortex tension, considering cadherin bonding between contacting cells in combination with down-regulation of cortical tension as important for cell–cell adhesion and redistribution of tension from individual cells to tissue boundaries (Manning *et al.*, 2010; Amack and Manning, 2012).

While the differential adhesion hypothesis and its variations were originally used to explain sorting during development, recent attempts have been made to apply it to cancer cells (Pawlizak *et al.*, 2015). Given the spatiotemporal heterogeneity of cells in cancerous masses, cell spatial organization, including sorting and segregation, may play a role in tumor progression (Foty and Steinberg, 2004). Indeed, a diverse population of cells exist in and around solid tumors, and the position of particular clonal and subclonal populations could have implications for whether malignant cells in a solid tumor breach the tumor basement membrane and invade surrounding stroma.

In recent work, robust sorting was observed in breast cell lines at various points along the epithelial-to-mesenchymal transition (EMT) (Pawlizak *et al.*, 2015). EMT is a key process through which noninvasive epithelial cells become invasion-competent. While EMT is a complex, multistep process, the simplest description of EMT involves cell loss of the epithelial marker E-cadherin and increases in N-cadherin and vimentin expression. Broadly, the process results in the loss of cellular adhesions and changes in the cytoskeleton that lead to increases in cellular contractility and invasive potential (Pastushenko and Blanpain, 2019). Loss of adhesivity allows cells to readily detach from tumors and enter the stromal environment. Upregulation of matrix metalloproteinases and Rho GTPase activity allows such cells to effectively degrade, actively remodel, and squeeze through pores in the surrounding extracellular matrix (ECM) during invasion (Sahai, 2005).

In the heterogeneous tumor microenvironment, interactions occur between cells at different stages along the epithelial to mesenchymal continuum, with a variety of consequences. For example, the presence of mesenchymal cells in a mixture of epithelial and mesenchymal cells may "fluidize" epithelial cells that otherwise tend to exhibit solid-like behavior, allowing them to effectively spill out into the local environment (Bi *et al.*, 2016; Gamboa Castro *et al.*, 2016; Atia *et al.*, 2018). Indeed, physical mechanisms underlying cancer invasion can be described through analogies with phase transitions (Malinverno *et al.*, 2017; Oswald *et al.*, 2017; Palamidessi *et al.*, 2019). Moreover, invasion-competent, mesenchymal cells are known to lead otherwise poorly invasive, epithelial cells in a leader–follower mode, with more invasive cells generating permissive paths in the surrounding ECM through which other cells follow (Gaggioli *et al.*, 2007; Carey *et al.*, 2013). Recent work has highlighted not only the importance of path generation by leader cells, but also that leader cells can physically pull follower cells through cadherin-based junctions (Labernadie *et al.*, 2017). The observation of robust sorting among cancer cells and the diverse set of interactions between cells at different points along the EMT encourages further study of whether spatial organization and boundary formation are important in cancer.

Here, we use a spheroid tumor model to identify factors that dictate spatial organization in heterogeneous multicellular aggregates, modulate these factors to control spatial organization in such aggregates, and explore the consequences of different spatial organizations within these aggregates on cell invasion. Six breast cell lines were chosen for this investigation: MDA-MB-231, MDA-MB-468, MDA-MB-436, MDA-MB-157, ZR-75-1, and MCF-10A. This panel contains a subset of cell lines that have been used in a previous breast cancer sorting study as well as additional cell lines to fully explore the range of sorting behaviors adopted by cell lines at various points along the EMT and with different degrees of overall aggressiveness as reported by genetic and functional assays (Vant Veer *et al.*, 2002; Kenny *et al.*, 2007; Pawlizak *et al.*, 2015; Ziperstein *et al.*, 2015). Cell lines were mixed in all 15 possible binary combinations to construct a sorting hierarchy for preference for the outside of the aggregate, and we rationalize the sorting hierarchy via consideration of spheroid compaction mechanisms, cell adhesion molecules, and cell contractility. We show that sorting can be predicted by compaction speeds of cell lines in isolation, which in turn is dictated by the presence of proteins involved in spheroid compaction and actomyosin contractility. Notably, actomyosin contractility plays different roles in cells using different modes of spheroid compaction. Using this knowledge, inhibitors are employed to control cell organization in aggregates in a subset of the cell lines investigated, as well as in aggregates composed of MCF-10A cells and an oncogenically transformed derivative thereof. Investigating the invasive properties of heterotypic spheroids with distinct spatial organizations reveals reciprocal interactions between invasive and noninvasive cells that depend on their initial position in the aggregate and shows that noninvasive cells restrain otherwise highly invasive cells in heterogeneous tumor models.

## RESULTS

### Cell sorting in binary aggregates

To investigate sorting behaviors in breast cancer, we chose a panel of cell lines displaying a variety of characteristics associated with overall aggressiveness and invasive capacity. The six cell lines employed and key characteristics thereof are shown in Table 1 (Vant Veer *et al.*, 2002; Kenny *et al.*, 2007; Kao *et al.*, 2009; Chavez *et al.*, 2010; Subik *et al.*, 2010; Lehmann *et al.*, 2011; Ziperstein *et al.*, 2015). Five of the cell lines are carcinomas, while one (MCF-10A) is benign and chosen to represent untransformed cells. Notably, cells range from more epithelial (MCF-10A, ZR-75-1) to more mesenchymal (MDA-MB-436, MDA-MB-231) in character (Blick *et al.*, 2008). It is of particular interest to explore the interactions between invasive and noninvasive cells, and so characteristics related to the invasive capacity of each cell line were considered (Table 1). Previously, gene expression profiles associated with invasive behavior of cancer cells were shown to be correlated with aggregate morphologies in three-dimensional (3D) culture in reconstituted basement membrane extract (Kenny *et al.*, 2007). Therefore, we chose cell lines spanning these morphological classes, with cell lines that form stellate aggregates typically associated with invasive behavior and those that form grape-like and mass-like aggregates displaying less invasive behavior.

Because aggregate morphology is only indirectly correlated with invasive capacity, a set of functional assays were also employed. In previous work, a collagen invasion assay that assesses cell invasion from spheroids in 3D collagen I matrices was shown to be correlated with additional measures of cell line aggression, including positive results in a 70-gene assay that has been successfully used to identify patients with early-stage breast cancers who are at a high risk of metastasis (Vant Veer *et al.*, 2002; Kao *et al.*, 2009; Ziperstein *et al.*, 2015). Of the six cell lines investigated here, MDA-MB-231 and MDA-MB-468 are the only ones that invade appreciably in this collagen invasion assay (Table 1; Supplemental Figure S1). To invade the collagen I–dominated stromal environment in vivo, breast cancer cells require both appropriate integrins for collagen attachment

| Cell line | Pathology | Aggregate morphology[a,b] | Subtype[b,c,d,e] | Receptor status (ER PR HER2)[b,c] | 70 Gene signature[f] | Collagen invasion capacity | Collagen contractile capacity |
|---|---|---|---|---|---|---|---|
| MDA-MB-231 | Infiltrating ductal carcinoma | Stellate | Basal B | — | + | ++ | ++ |
| MDA-MB-436 | Infiltrating ductal carcinoma | Stellate | Basal B | — | + | – | – |
| MDA-MB-157 | Infiltrating medullary carcinoma | Stellate | Basal B | — | – | – | ++ |
| MDA-MB-468 | Adenocarcinoma | Grape-like | Basal A | — | + | + | + |
| ZR-75-1 | Infiltrating ductal carcinoma | Mass | Luminal A | ++–/+–– | – | – | + |
| MCF-10A | Fibrocystic, benign | Mass | Basal B | — | – | – | – |

Information on aggregate morphology from (a) Ziperstein *et al.*, 2015, and (b) Kenny *et al.*, 2007; subtype from (b) Kenny *et al.*, 2007, (c) Lehmann *et al.*, 2011, (d) Chavez *et al.*, 2010, and (e) Subik *et al.*, 2010; receptor status from (b) Kenny *et al.*, 2007, and (c) Lehmann *et al.*, 2011; and 70 gene signature from (f) Kao *et al.*, 2009. Information on collagen invasion capacity and collagen contractile capacity are provided in Supplemental Figure S1.

**TABLE 1:** Cell line characteristics.

and sufficient actomyosin contractility to facilitate migration and associated matrix remodeling. While cellular contractility alone is not sufficient for invasion, it is necessary and common to invasive cell types (Ziperstein *et al.*, 2015). Therefore, we also characterized the combination of presence of relevant integrins and cellular contractility via collagen I gel contraction assays (Table 1; Supplemental Figure S1). The two invasive cell lines as well as ZR-75-1 and MDA-MB-157 were found to quite effectively contract the collagen I gels while MDA-MB-436 and MCF-10A display only weak collagen contractile capacity.

To determine sorting behavior, cell lines were tagged with the fluorescent dyes CellTracker Green and CellTracker Orange and mixed 1:1 to create heterotypic aggregates intended to mimic the heterogeneous subpopulations of cancer cells within a solid tumor (Figure 1; Supplemental Figure S2). Before aggregate formation experiments, dyes were tested in spheroid invasion and aggregate sorting assays, which showed that the dyes had no observable impact on cell behavior and that dye transfer between cell lines was negligible (Supplemental Figure S3). For all cell line combinations, the sorting behavior was categorized by which cell line preferred the outside of the aggregate by visual inspection (Table 2). Sorted states were classified as complete, partial, or mixed, where complete corresponds to cells that sorted into two distinct populations, partial corresponds to a configuration where one type of cell is enveloped by the other but neither cell type coalesces into a single entity, and mixed corresponds to a case where no appreciable sorting occurs (Figure 1, a–c). Quantitative analysis was also undertaken to confirm the qualitative assessments.

We quantitatively analyzed images during and after sorting using a method described in Cochet-Escartin *et al.* (2017), which utilizes two metrics, blob size and the boundary ratio. Briefly, blob size is a measure of the size of the distinct spatial regions into which cells coalesce, a measure that has been used in theoretical descriptions of fluid phase separation (Fan *et al.*, 2016), while boundary ratio refers to the normalized length of the boundary between two distinct cell types. Images of the developing aggregates were taken every 12–24 h over 2–3 d and then postprocessed to determine sorting metrics (Supplemental Figure S4). In initial images of cell mixtures, closely spaced, individually distinguishable single cells of alternating types (and, therefore, colors) are present. These small spatial domains are associated with high-frequency components in the Fourier transformed image, and therefore small blob size. As sorting progresses, cells of a particular type coalesce into larger aggregates (Figure 1, d and e), and correspondingly lower-frequency components emerge in the analyzed images. This leads to an increase in blob size for cell mixtures that undergo appreciable demixing. The boundary ratio decreases concomitantly over the course of sorting as many small islands of a particular cell type, each with interfaces with cells of the other type, become fewer, larger groups of cells with smaller interfacial area.

Sorting behavior as described by these metrics is expected to follow power law behavior (Cochet-Escartin *et al.*, 2017). Therefore, the values of blob size and boundary ratio as they evolved over time (Figure 1, f and g) were fitted to power laws, and the resulting fitting exponents were compared across sorting categories. Analysis revealed blob size fitting exponents of $0.3 \pm 0.1$, $0.25 \pm 0.08$, and $0.06 \pm 0.02$ for spheroids categorized via visual observation as complete, partial, and mixed cases, respectively (mean ± SD). A similar trend was observed for boundary ratios, with fitting exponents of $-0.6 \pm 0.3$, $-0.5 \pm 0.2$, and $-0.1 \pm 0.1$, for complete, partial, and mixed sorting. The exponents obtained here were similar to, although smaller than, previously published values, which is likely related to the fact that the cells investigated in this study demonstrate slower sorting than do cells during germ layer sorting. Blob size exponents did not indicate significant differences between sorting rates in cases of complete and partial sorting as judged by visual inspection, while boundary ratio exponents did (Figure 1, h and i). However, both blob size and boundary ratio exponents were found to be moderately strongly correlated among all sorting combinations, suggesting that they report on similar aspects of sorting dynamics (Supplemental Figure S5). Importantly, both blob size and boundary ratio exponents showed a clear difference between sorting rates for complete/partially sorted cases and mixed cases, demonstrating that this quantitative measure accurately reflects the qualitative assessments and can distinguish between cases that do or do not appreciably sort. Blob size and boundary ratio can also be used to determine degree of sorting via total change in blob size and boundary ratio for each sorting case. Again, significant differences were found between combinations that do and do not sort, as well as between complete and partially sorted cases (Figure 1, j and k).

From the data presented in Figure 1 and summarized in Table 2, the sorting hierarchy is ranked as MDA-MB-468 > MDA-MB-231 > MDA-MB-436 = ZR-75-1 > MDA-MB-157 > MCF-10A, with the cells sorting to the outside (complete or partially) of any cell line to its right except for the case of MDA-MB-436 and ZR-75-1, which result in mixed aggregates. MDA-MB-468 is included in the sorting

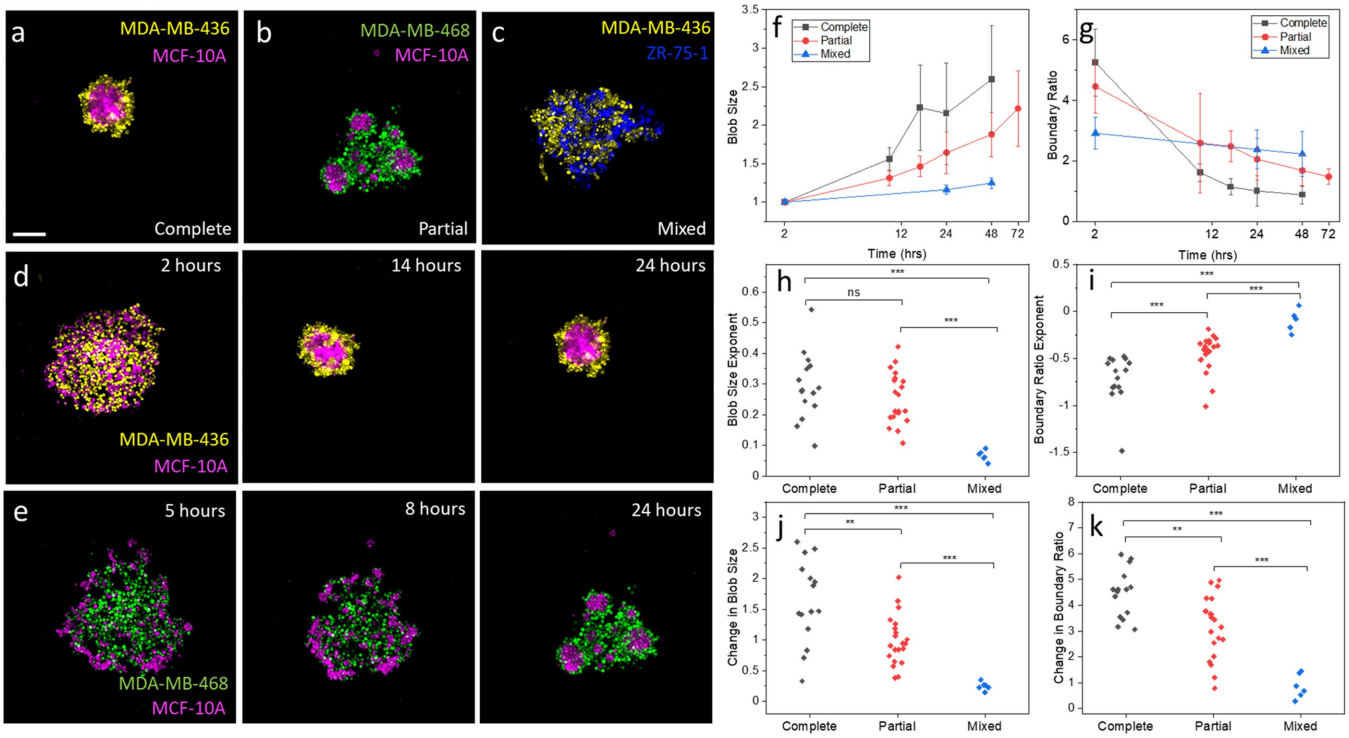


**FIGURE 1:** Representative coculture of sets of breast cell lines showing (a) complete sorting (MDA-MB-436 [yellow] and MCF-10A [magenta]), (b) partial sorting (MDA-MB-468 [green] and MCF-10A [magenta]), or (c) no sorting (mixed) (MDA-MB-436 [yellow] and ZR-75-1 [blue]) following 24 h in suspension culture. Final sorted states are shown for all cell line combinations in Supplemental Figure S2. (d) Time course demonstrating the sorting process for a completely sorted case (MDA-MB-436 [yellow] and MCF-10A [magenta]), with images taken at 2, 14, and 24 h. (e) Time course demonstrating the sorting process for a partially sorted case (MDA-MB-468 [green] and MCF-10A [magenta]), with images taken at 5, 8, and 24 h. (f, g) Evolution of (f) blob size and (g) boundary ratio over the course of the sorting process averaged over all combinations in each sorting category. Traces are depicted as black, red, and blue lines for complete sorting, partial sorting, and mixed cases, respectively. (h, i) Fitting exponents from (h) blob size and (i) boundary ratio exponents for all combinations, obtained by fitting traces shown in f and g. Change in (j) blob size and (k) boundary ratio over the entire sorting process for each combination. Scale bar = 200 μm. In h–k, ns indicates not significant, * indicates $p < 0.05$, ** indicates $p < 0.01$, and *** indicates $p < 0.001$. Significance was determined with a *t* test or Mann–Whitney test depending on the normality of data (see *Materials and Methods* for details, $n = 2$–3 for each combination).

hierarchy, though we note that its behavior is distinct from that of other cell lines: while it sorts to the outside of most other cells, it is highly resistant to compaction, does not result in full sorting with any cell line, and results in a mixed aggregate when combined with MDA-MB-436 cells. Overall, the sorting hierarchy reveals that the more invasive, transformed cell lines display a preference for the outside of the aggregate, though we note that the sorting hierarchy is not fully correlated with any characteristic reported in Table 1.

## Spheroid compaction mechanisms

Given that no factors summarized in Table 1 fully correlate with the sorting hierarchy, to identify factors that drive aggregate sorting, first, simple aggregation experiments were conducted for each cell line in isolation (Figure 2; Supplemental Figure S6). Cell lines exhibited a wide range of compaction speeds and tightness of the final aggregates, and we categorized cell lines as loose aggregate formers or spontaneous spheroid formers through visual inspection in

| | MDA-MB-468 | MDA-MB-231 | MDA-MB-436 | ZR-75-1 | MDA-MB-157 | MCF-10A |
|---|---|---|---|---|---|---|
| MDA-MB-468 | – | | | | | |
| MDA-MB-231 | 468[a] | – | | | | |
| MDA-MB-436 | Mix | 231 | – | | | |
| ZR-75-1 | 468[a] | 231[a] | Mix | – | | |
| MDA-MB-157 | 468[a] | 231[a] | 436 | 751[a] | – | |
| MCF-10A | 468[a] | 231 | 436 | 751 | 157 | – |

The cell line name in the table for each combination indicates the cell line with a preference for the outside of the aggregate. Cell line names within the table are abbreviated with the final three alphanumeric characters in their full names.
[a]Partial sorting.

**TABLE 2:** Sorting results for all cell line combinations.

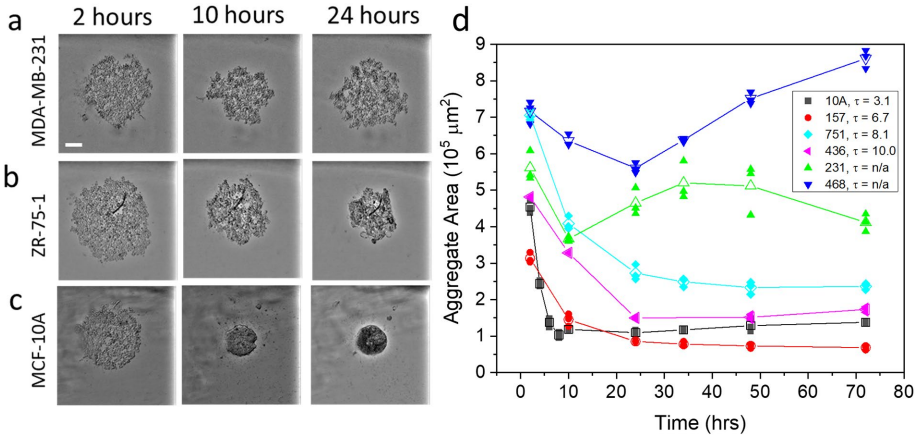


**FIGURE 2:** Aggregate compaction dynamics of representative cell lines. Representative transmitted light images of (a) MDA-MB-468, (b) ZR-75-1, and (c) MCF-10A at 2, 10, and 24 h in suspension culture. Representative images for all cell lines at 2, 10, 24, and 72 h are shown in Supplemental Figure S6. Scale bar in a is 200 μm and applies to all images. (d) Aggregate area (measured from a single confocal slice at the widest part of the aggregate) as a function of time for all cell lines over 72 h. Error bars represent SD ($n = 3$ for each cell line). For cells that compact well (MDA-MB-436, ZR-75-1, MDA-MB-157, and MCF-10A), the evolution of aggregate area was fitted to the form $A^*e^{(-t/\tau)} + c$, and the characteristic compaction time in hours, τ, is reported in the legend. Supplemental Figure S7 shows best fits to the data. n/a is used for cell types that do not compact well and cannot be fitted to this form.

accordance with previous work (Ivascu and Kubbies, 2007). The key distinction is that in loose aggregate formers, individual cells can be distinguished even after compaction has proceeded for 72 h, while in spontaneous spheroid formers this is not the case (Supplemental Figure S6). Loose aggregate formers include MDA-MB-468, MDA-MB-231, MDA-MB-436, and ZR-75-1. Among these cell lines, MDA-MB-468 and MDA-MB-231 formed only loose, irregular aggregates even at long times, with MDA-MB-468 cells never evolving into a tighter aggregate than that present 2 h after plating. The behavior of MDA-MB-468 cells in isolation shows that these cells possess virtually no adhesive character in suspension culture, consistent with their behavior in heterotypic aggregates, where these cells typically sort outside other cells but never coalesce with each other, as seen in Supplemental Figure S2. MDA-MB-436 and ZR-75-1 cells compacted relatively rapidly into rather small aggregates, but single cells could be easily distinguished, and the aggregates remained irregularly shaped. Loose aggregate formers could be induced to form tightly packed, compact spheroids through supplementation of ECM components, such as basement membrane extract (BME) or collagen (Supplemental Figure S8), a common approach to making spheroids from such cell lines (Ivascu and Kubbies, 2006, 2007; Froehlich *et al.*, 2016). Spontaneous spheroid formers, as the name implies, formed tight spheroids without the need for additional supplementation. MCF-10A cells formed the most homogeneous spheroids: they were nearly perfectly spherical and displayed a smooth boundary with the surrounding media. MDA-MB-157 cells were comparably slow to compact but formed tight spheroids over the course of 48 h. To compare compaction speeds across cell types, the characteristic compaction time, τ, was obtained from exponential fits to the reduction in aggregate area over time (Supplemental Figure S7), and these are reported in Figure 2 for all cell lines except MDA-MB-468 and MDA-MB-231, which did not show monotonically decreasing aggregate area over time. We find that characteristic compaction times correlate with the sorting hierarchy; compaction speed dictates sorting preference of heterotypic aggregates in coculture, and sorting appears to be driven by the aggregation of the more efficiently compacting cell line (Supplemental Video S1).

To rationalize the sorting behaviors of these cell lines, we return to the differential adhesion hypothesis. Because the simplest formulations of the differential adhesion hypothesis focused on adhesion protein types and expression to explain cell sorting (Foty and Steinberg, 2005; Steinberg, 2007), we first considered the roles of cell adhesion proteins relevant to aggregate formation. Although cadherins are the traditional cell–cell adhesion proteins, due to the aberrant cadherin expression observed in many cancers, additional proteins were considered. In previous work on breast cancer cell lines, compaction mechanisms were organized into three categories: $\beta_1$ integrin, E-cadherin, or N-cadherin mediated (Ivascu and Kubbies, 2007). To test the importance of these proteins in aggregate formation in the cell lines investigated here, antibody inhibition, small interfering RNA (siRNA) knockout, and calcium depletion were used (Table 3; Supplemental Figure S8). For these studies, compaction was facilitated through the addition of BME to loose aggregate formers to encourage spheroid formation on a timescale similar to spontaneous spheroid formers so that inhibitory effects could be clearly assessed. MDA-MB-468 cells were previously reported to require dual $\beta_1$ integrin and E-cadherin inhibition to disrupt spheroid formation, while inhibition of only one had no effect (Ivascu and Kubbies, 2007). However, we found that MDA-MB-468, along with MDA-MB-231 and MDA-MB-436 cells, rely primarily on $\beta_1$ integrin to mediate spheroid formation, as shown through $\beta_1$ integrin antibody inhibition and siRNA knockdown, both of which clearly disrupted spheroid formation (Supplemental Figure S8). Although integrins are typically thought of as mediating cell–ECM contacts and not cell–cell contacts, there are reports of strong integrin-based cohesion in cells. Reportedly, integrin-based adhesions can even be stronger than cadherin-based ones (Foty and Steinberg, 2004; Winklbauer, 2019). Specifically, $\alpha_5\beta_1$ integrin has been shown to play a significant role in tissue cohesion through intercellular fibronectin adhesion (Robinson *et al.*, 2004). In a $\beta_1$ integrin–mediated spheroid formation process, it has been proposed that spheroid formation occurs in three steps (Lin *et al.*, 2006). First, integrins adhere to supplemental ECM intercalated between cells to create integrin–ECM linkages. Following assembly of a loose aggregate, a delay period follows in which cadherins can be up-regulated and/or accumulate. This is followed by a compaction step mediated by cadherins that results in a tightly packed spheroid. In this type of compaction, ECM molecules act as physical linkers, and an ECM network can be seen within the spheroid. Indeed, we found plentiful active $\beta_1$ integrin throughout MDA-MB-231 spheroids formed with either BME or acid-solubilized collagen I (Figure 3, a and b). The antibody labeling of active $\beta_1$ integrin (antibody clone 12G10) relies on binding to an epitope that is accessible for integrin only in the extended conformation. This conformation is energetically favorable in the ligand-bound state, giving a

Sorting Hierarchy

| Cell line | Compaction mediator | Method |
|---|---|---|
| MDA-MB-468 | $\beta_1$ Integrin[a] | AB, siRNA |
| MDA-MB-231 | $\beta_1$ Integrin[a] | AB, siRNA |
| MDA-MB-436 | $\beta_1$ Integrin | AB |
| ZR-75-1 | $\beta_1$ Integrin and E-cadherin | AB |
| MDA-MB-157 | Cadherin | $Ca^{2+}$ depletion |
| MCF-10A | E-cadherin | AB, $Ca^{2+}$ depletion |

Cell lines are listed in an order consistent with the sorting hierarchy. AB = antibody inhibition.
[a]Mediators also found in Ivascu and Kubbies (2007).

**TABLE 3:** Compaction mediators.

very high probability that integrins in this conformation are ligand bound (Li *et al.*, 2017). Even with ECM supplementation, a spontaneous spheroid former such as MCF-10A did not show integrin activation throughout the interior of the spheroid, but rather only on the cells at the spheroid–media interface, consistent with integrin activity being neither necessary nor used during formation (Figure 3c). Quantification of the ratio of fluorescence of active $\beta_1$ integrin at interior cell–cell contacts relative to that at surface cell contacts with media revealed that MDA-MB-231 cells have a ratio nearly 10 times higher than that of MCF-10A cells formed under the same conditions (Supplemental Figure S9).

Among the spontaneous spheroid formers, MCF-10A was found to rely on E-cadherin for compaction, with E-cadherin inhibitory antibody and 1 mM ethylene glycol-bis(β-aminoethyl ether)-*N*,*N*,*N*′,*N*′-tetraacetic acid (EGTA) supplementation each preventing aggregation, with the latter depleting calcium required for cadherin activity (Lin *et al.*, 2006) (Supplemental Figure S8). Moreover, MCF-10A spheroids exhibited strong E-cadherin immunostaining throughout, consistent with a cadherin-based compaction mechanism (Figure 3d). Notably, cells at the surface of the spheroid and in contact with the media appeared to lack E-cadherin. MDA-MB-157 cells lack E-cadherin, but these spheroids still underwent efficient compaction that could be disrupted through calcium depletion with EGTA, indicating a cadherin-dependent mechanism (Lin *et al.*, 2006). It is important to note that while spontaneous formers were not supplemented with ECM components during formation, supplementation did not prevent compaction from occurring preferentially via a cadherin-dependent mechanism. Spheroids formed with BME under $\beta_1$ integrin inhibition still efficiently compacted (Supplemental Figure S8). ZR-75-1 cells are unique in that these cells underwent compaction mediated by both $\beta_1$ integrin and E-cadherin. Individual inhibitions of E-cadherin and $\beta_1$ integrin were both effective in disrupting aggregate formation to an extent, with the most effective inhibition accomplished by dual inhibition (Supplemental Figure S8). Generally, among the cell lines investigated, spontaneous spheroid formers were found to rely on cadherin-mediated adhesions for rapid and tight compaction, while loose aggregate formers showed significant $\beta_1$ integrin involvement. Cells using the $\beta_1$ integrin–dependent

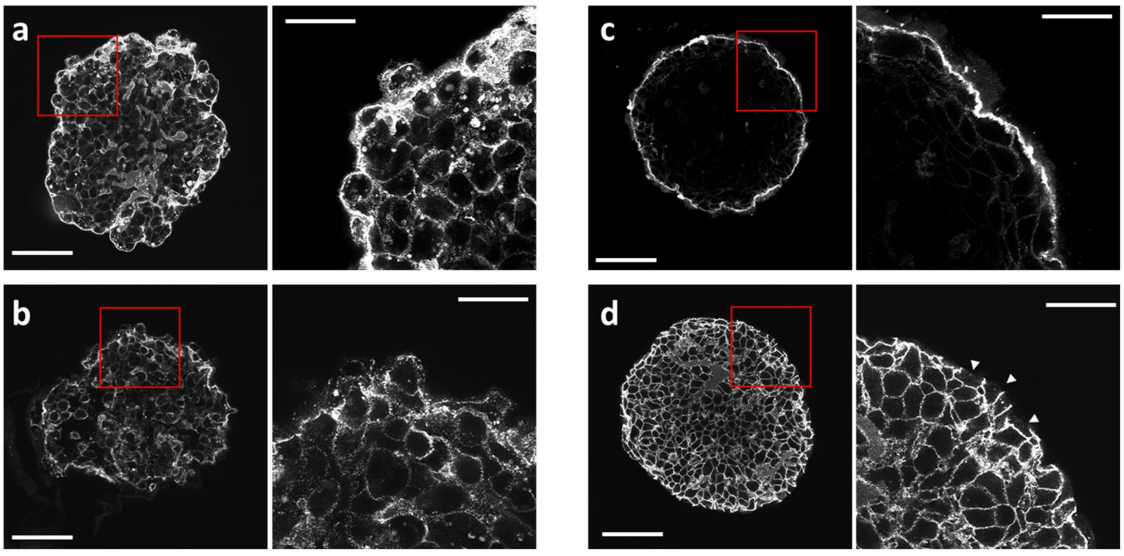


**FIGURE 3:** MDA-MB-231 spheroids formed with (a) BME (0.2575 mg/ml) or (b) acid-solubilized (AS) collagen I (10 μg/ml) display active $\beta_1$ integrin throughout the spheroid, indicating many cells binding ECM as a network is formed between the cells. (c) MCF-10A spheroids formed with the same amount of AS collagen I supplementation display large amounts of active integrin only on the outer rim of the spheroid. (d) MCF-10A spheroid stained for E-cadherin shows strong signal throughout, confirming the reliance of MCF-10A spheroids on cadherins for tight compaction and demonstrating the ability of antibodies to penetrate dense spheroids efficiently. Cells at the spheroid–media interface lack E-cadherin, as indicated by the white arrowheads. All images are single slices through the middle of spheroids. Scale bars = 50 μm for full spheroids at the left and 20 μm for zoomed-in regions at the right.

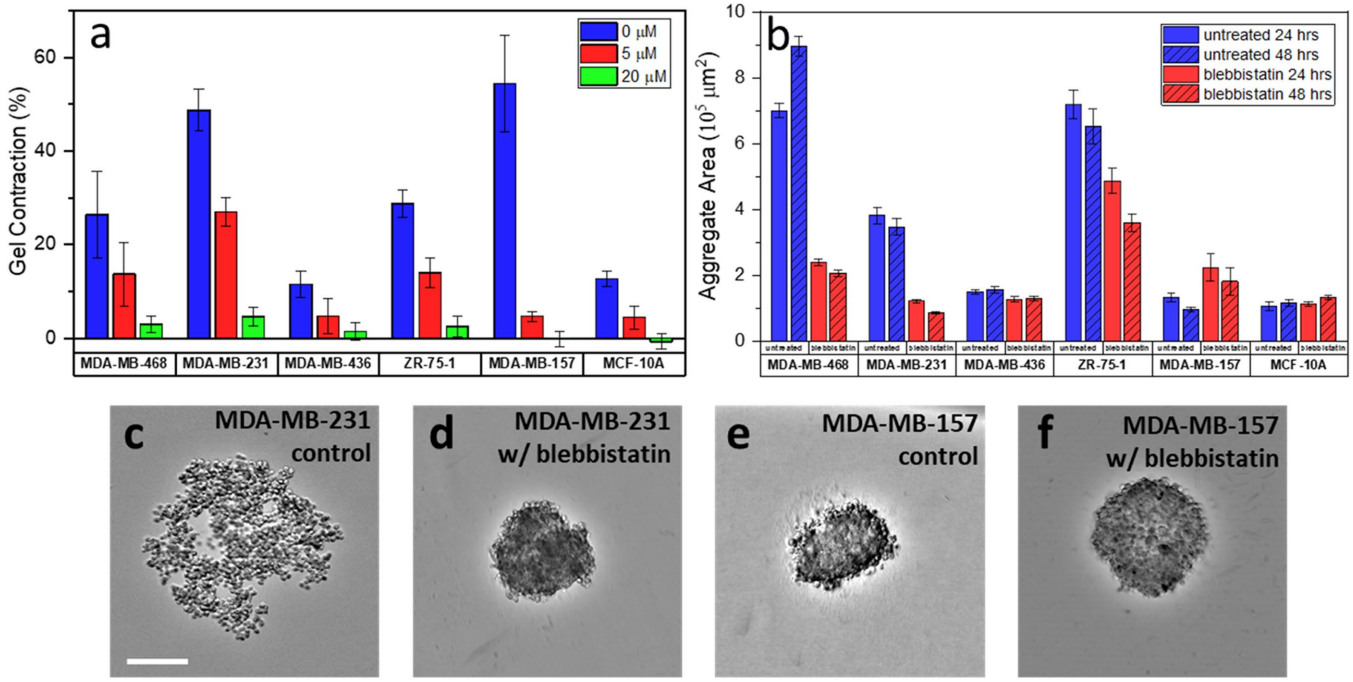


FIGURE 4: (a) Gel contraction for untreated cells and those treated with blebbistatin at 5 and 20 μM, all assessed after 4 h ($n$ = 6; error bars show SDs). (b) Aggregate area for untreated cells and those treated with 20 μM blebbistatin ($n$ = 10–12 for each cell line; error bars show SDs) assessed at 24 h (solid bars) and 48 h (cross-hatched bars). (c–f) Representative transmittance images of (c, d) MDA-MB-231 and (e, f) MDA-MB-157 aggregates that are (c, e) untreated or (d, f) treated with 5 μM blebbistatin for 48 h. Scale bar = 200 μm.

compaction processes possess inherently lower adhesivity and display slower compaction than cells utilizing cadherin-based compaction, which in turn impacts sorting order. Indeed, the rapid compaction exhibited by cadherin-mediated spheroid formers results in their preference for the inside of mixed aggregates and determines their position in the sorting hierarchy (Table 3).

### Impact of actomyosin contractility on sorting

To further elucidate the factors driving the sorting patterns observed, the role of actomyosin contractility in aggregate formation was evaluated. Cells were treated with blebbistatin to modulate actomyosin contractility levels during spheroid formation. Blebbistatin is a selective myosin II ATPase inhibitor that reduces cellular contractility. To observe the effects of blebbistatin on cell behavior, gel contraction assays were performed at concentrations of 5 and 20 μM, which provide intermediate and high levels of contractility inhibition, respectively (Figure 4a). All cell lines showed at least 50% less contraction with 5 μM treatment, with MDA-MB-157 particularly strongly inhibited (~90%) at that concentration, and all cell lines showed a reduction of gel contraction ability by >95% at 20 μM. Aggregate compaction measurements were then undertaken over 72 h under 20 μM blebbistatin treatment. Interestingly, these experiments revealed a distinct role for active contractility among cell lines utilizing different compaction mechanisms. Compaction of cell lines in which aggregation was driven by cadherins was disrupted by blebbistatin, with MDA-MB-157 aggregates much more noticeably disrupted than those of MCF-10A in terms of change in aggregate size (Figure 4, b, e, and f). In contrast, in the integrin-dependent spheroid formers MDA-MB-231 and MDA-MB-468, compaction was remarkably increased by the addition of 5 and 20 μM blebbistatin to the media, resulting in spheroids comparable to those formed by supplementation with BME (Figure 4, b–d; Supplemental Video S2). ZR-75-1 and MDA-MB-436 cells showed more modest compaction enhancement upon the addition of blebbistatin to the culture media, likely owing to the already considerably compact nature of the untreated aggregates.

From the data presented in Figure 4, it is clear that contractility plays a fundamentally different role in the cell lines in which compaction is driven primarily by integrins versus by cadherins. Cell lines with $\beta_1$ integrin involvement respond favorably with respect to spheroid formation upon reduction of contractility. This is an unexpected result, as contractility is necessary for spheroid formation and facilitates the development of mature cell–cell contacts in developing aggregates (Yamada and Nelson, 2007; Maître *et al.*, 2012). To confirm that this compaction-enhancing effect is due to modulation of cellular contractility and not off-target effects of blebbistatin, cells were treated with the inactive enantiomer (+)-blebbistatin. Treatment with (+)-blebbistatin did not have an appreciable impact on MDA-MB-231 compaction. In contrast, using other methods to reduce contractility resulted in similarly enhanced compaction to that achieved via (-)-blebbistatin (Supplemental Figure S10). Treating MDA-MB-231 with 10 μM Y27632, an inhibitor that targets Rho-associated protein kinase p160ROCK (Uehata *et al.*, 1997), resulted in compact aggregates similar to those formed with blebbistatin treatment. Compaction of MDA-MB-231 cells was also enhanced by serum starvation, which decreases Rho activation, as well as with treatment with the myosin light chain kinase inhibitor ML-7.

We note that in MDA-MB-231 cells treatment with blebbistatin at or greater than 5 μM resulted in efficient compaction (Supplemental Figure S10), suggesting that a moderate decrease in contractility is sufficient to encourage spheroid formation. Higher concentrations did not show an increased effect. Phototoxic or cytotoxic effects of long-term blebbistatin incubation were also ruled out by treating

cells with two more recently developed photostable and noncytotoxic derivatives, para-nitro and para-aminoblebbistatin (Supplemental Figure S10) (Képiró *et al.*, 2014; Várkuti *et al.*, 2016). In addition to reduced phototoxicity, para-aminoblebbistatin's improved solubility allows a roughly 10-fold increase in concentration to be achieved. Treatment of MDA-MB-231 with 100 μM para-aminoblebbistatin resulted in less effective compaction compared with lower concentrations, suggesting diminished ability to form spheroids when contractility is heavily reduced.

To more closely examine the potentially differential effects of relaxing actomyosin contractility on spheroid compaction, we focused on two cell lines where contractility reduction had an opposite effect—MCF-10A and MDA-MB-231. While the change in size of MCF-10A aggregates under blebbistatin treatment was relatively modest (Figure 4b), a marked change in cell morphology at the perimeter of the spheroid was evident, with a transition from extended or stretched cells to more rounded cells (Figure 5, a and b) while interior cells were smaller and more polygonal, regardless of spheroid preparation conditions (Supplemental Figure S11a). For the untreated spheroid, phalloidin staining revealed a bright actomyosin cable along the smooth spheroid boundary; this feature was absent in the spheroid treated with blebbistatin. Stretched surface cells have been observed in zebrafish and associated with high contractile forces and tissue surface tension (Krieg *et al.*, 2008; Manning *et al.*, 2010). The stretched morphology compared with interior cells suggests regulation of contractility such that cortical tension is high at cell–media interfaces compared with interior cell–cell interfaces.

To quantitatively analyze the effects of contractility inhibition, the cell shape index—ratio of cell perimeter to square root of area—was measured, as cell shape can reflect competition between cell adhesion and cortical tension within a tissue (Bi *et al.*, 2016; Yang *et al.*, 2017). For a given cell, the shape index has a minimum value of ~3.54, indicating a perfect circle, with increasing values indicating more-elongated shapes. Untreated MCF-10A spheroids display a smooth boundary with the surrounding media, which results in a stark difference in cell shape index between interior and exterior cells (Figure 5d), with a median of 3.9 for interior cells and 5.0 for the more-extended cells found at the surface. Upon treatment with 20 μM blebbistatin, a subtle change in cell morphology was observed. Surface cells appeared rounder, and the median cell shape index shifted from 5.0 to 4.7. Upon increasing the blebbistatin concentration to 40 μM, more obvious spheroid disruption was observed, with a further shift in median surface shape index to 4.3 and a distribution of cell shapes that is significantly different from those of the untreated spheroid (Figure 5e). Aggregates lost the smooth boundary with the surrounding environment and became more irregular in shape. It appears that contractility inhibition lowers the tissue surface tension, as evidenced by the more irregular interfacial boundary. Further rounding up of surface cells was observed when forming spheroids with BME, which encapsulates cells in a layer of ECM (Figure 5e; Supplemental Figure S11b) separating them from the media and shifting the shape index to even lower values. In BME-formed spheroids, we hypothesize that cell rounding is driven by cells being presented with ECM and thus favorable attachment points at the surface of the spheroid, no longer encouraging cell stretching to maximize cell–cell adhesions relative to cell–medium contact. For MDA-MB-231 aggregates, blebbistatin had a very similar effect on cell shape, encouraging cell rounding at spheroid edges (Figure 5, c and e). Blebbistatin-treated MDA-MB-231 spheroids displayed surface cells with shape indices similar to those found in BME-formed MCF-10A spheroids (Figure 5c; Supplemental Figure S11), the condition that encouraged the most cell rounding. While blebbistatin treatment does encourage MDA-MB-231 spheroid formation, it appears to cause the same cell rounding that it causes in MCF-10A spheroids. Unlike surface cells, interior cells did not show significantly different cell shape distributions across either spheroid formation conditions or across cell lines (Figure 5f; Supplemental Figure S11a).

The fact that exterior cell shape varies significantly across cell type and spheroid preparation conditions while interior cell shape does not is related to the ability of cells to translate cortical tension of individual cells into the surface tension of the multicellular aggregate. As discussed previously, the cortical tension of individual cells has been shown to correlate well with sorting, as well as with overall aggregate surface tension (Krieg *et al.*, 2008). Such a redistribution is contingent on stable cell–cell coupling; in the absence of such coupling, contractile cells displaying high cortical tension tend to pull away from each other due to high levels of interfacial tension between cells. In the presence of such coupling, the cortical tension is redistributed toward the outside of the aggregate, resulting in lower cell–cell cortical tension and higher cortical tension at cell–media interfaces, that is, a mechanical polarization at the edge of the tissue (Amack and Manning, 2012). The reorganization of adhesive and cytoskeletal machinery to accomplish this is an important step in aggregate formation. We find that only in cell lines in which compaction is driven by cadherins can cortical tension be redistributed effectively.

To further investigate the role of mechanical polarization in the cell lines studied here, we examined phospho-myosin light chain localization in spheroids. Antibody staining revealed high levels of myosin phosphorylation (and therefore cortical tension) at the boundaries of the aggregate in spheroids constructed from both cell lines (Figure 5, g and h). MCF-10A cells displayed strong localization of phosphorylated myosin at the spheroid surface, indicating that sufficient contractile ability is present even under blebbistatin treatment and suggesting that redistribution of tension within the aggregates takes place following initial cell-cell adhesion. MDA-MB-231 cells displayed obvious differences in spheroid character when formed using different methods. MDA-MB-231 spheroids formed with BME displayed integrin activation throughout (Figure 3a) indicating the presence of many ECM-integrin contacts between cells. Upon removal of BME following spheroid formation, spheroids displayed phospho-myosin staining between interior cells (Figure 5h), indicating regions of high cortical tension between cells. Taken together, these findings suggest that ECM-integrin contacts are the main source of adhesion in such spheroids and, in the absence of an ECM network to hold the spheroid together, effective repulsions between cells resulting from high cellular contractility reduce spheroid cohesion, consistent with the lack of compaction seen in these cells in the absence of supplementation (Figure 2, a and d; Supplemental Figure S6b). In contrast to MDA-MB-231 spheroids formed in the presence of BME, MDA-MB-231 spheroids formed in the presence of blebbistatin displayed phospho-myosin staining near identical to that of MCF-10A spheroids (Figure 5h), indicating a more robust, mechanical coupling of cells that allows tension redistribution to occur to the aggregate boundary. In both MCF-10A and MDA-MB-231 cells, it appears that contractility inhibition by blebbistatin is partial, leaving cells with sufficient levels of contractility to mediate aggregate formation but not enough to cause surface cell stretching. Notably, the threshold for effective compaction of MDA-MB-231 cells could be accomplished at blebbistatin concentrations that reduce contractile ability by roughly half, as measured through gel contraction assays (Figure 4; Supplemental Figure S10). Interestingly, spheroid formation was still quite

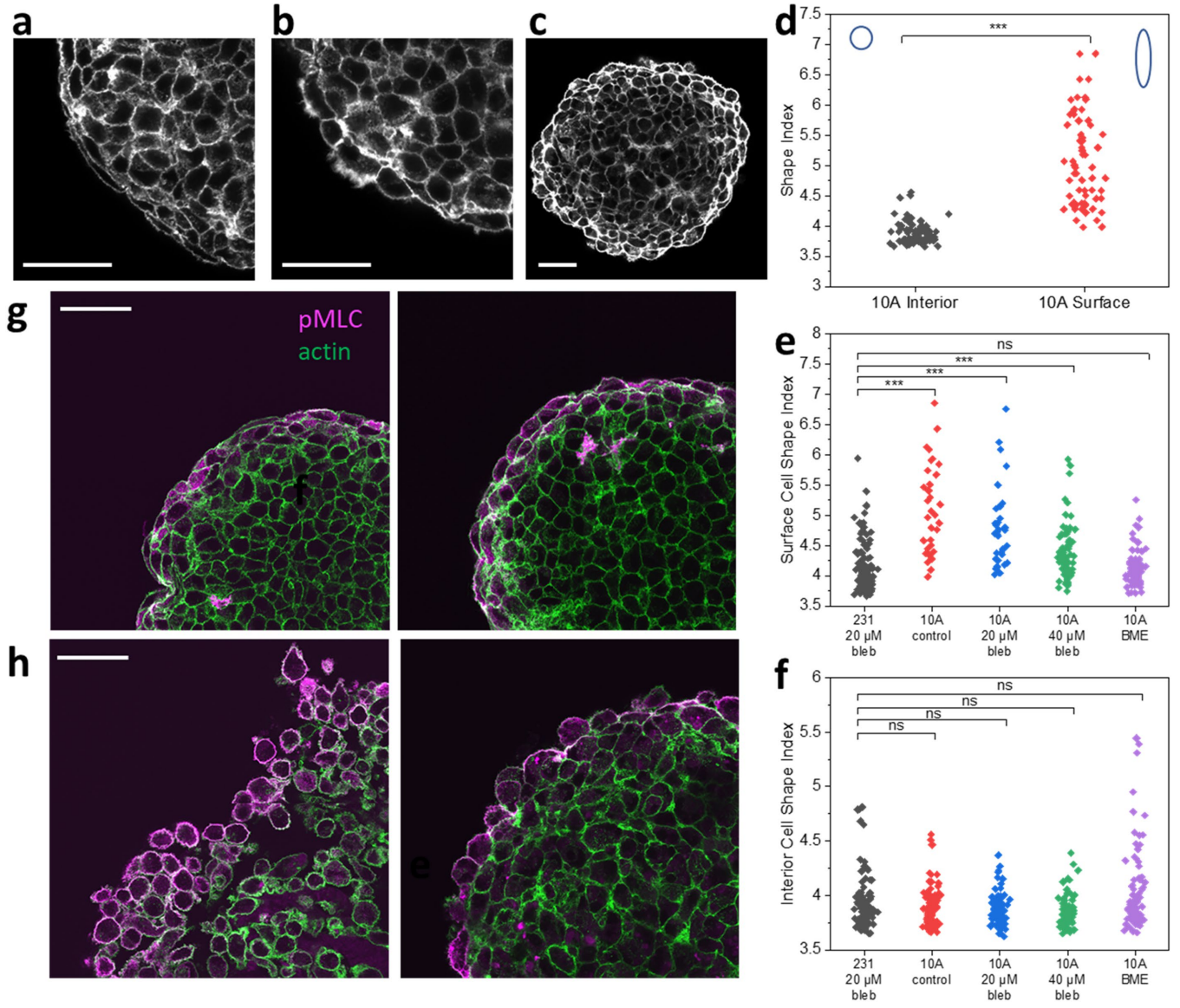


FIGURE 5: (a) Actin immunostaining of untreated MCF-10A spheroid shows surface cells with stretched morphology. (b) Actin immunostaining of an MCF-10A spheroid treated with 20 μM blebbistatin shows more-rounded surface cells. (c) Actin immunostaining of an MDA-MB-231 spheroid treated with 20 μM blebbistatin shows similarly rounded cells. Scale bars are 20 μm in a and b and 40 μm in c. (d) Dimensionless shape index (SI) (perimeter/[Area]$^{0.5}$) for cells in the spheroid shown in (a) reveals that interior cells have significantly smaller shape indices than cells at the spheroid surface. A circle (with SI = 3.5) and an ellipse with SI = 5.0 are shown for context. (e) Surface cell shape index as a function of treatment with blebbistatin or supplementation with BME during spheroid compaction. (f) Interior cell shape index as a function of treatment with blebbistatin or supplementation with BME during spheroid compaction. ns indicates not significant, and *** indicates $p < 0.001$. Differences between shape distributions are determined by Kolmogorov–Smirnov tests. $n \geq 34$ for each condition. (g, h) Immunostaining of phospho-MLC (pMLC) as a proxy for cortex tension. (g) MCF-10A spheroid formed (left) without supplements and (right) treated with 5 μM blebbistatin show similar staining patterns (pMLC magenta, actin green). (h) MDA-MB-231 spheroids (left) formed with BME and (right) when treated with 5 μM blebbistatin show enhanced cell–media relative to cell–cell pMLC staining when treated with blebbistatin. In g and h, images are single slices through the middle of the spheroid. Scale bars in g and h are 30 μm.

effective at higher blebbistatin concentrations, where gel contraction was nearly abolished. This suggests that only low levels of contractility are required for spheroid formation and is consistent with the fact that relatively noncontractile cells such as MCF-10A can display highly stretched surface cells in spheroids. MDA-MB-231 compaction was reduced at sufficiently high inhibitor concentrations, suggesting that there is a point where cellular contractility can be too heavily reduced, beyond the detection limit in the contraction assays (Supplemental Figure S10f).

### Inverted static and dynamic aggregate sorting

Knowledge of the importance of adhesion molecules for cell line compaction and the differential effects of contractility inhibition across cell lines suggests that sorting may be controlled by

selectively inhibiting adhesion proteins and/or modifying actomyosin contractility. Notably, the distinct effect of modifying actomyosin contractility can be exploited to reverse preferences for the outside of the aggregate. For example, in the case of MDA-MB-231/MCF-10A coculture aggregates, MDA-MB-231 normally sorts to the outside of the aggregate (Supplemental Figure S2e). Upon application of blebbistatin during compaction in suspension culture, which has a compaction-promoting effect in MDA-MB-231 cells and a mildly spheroid disrupting effect in MCF-10A cells, the aggregates became more mixed, with notable instances of trilayered spheroids, with MDA-MB-231 cells present both on the outside and in the inner core (Figure 6a). Upon additional application of an inhibitory E-cadherin antibody, a near-complete sorting flip was achieved (Figure 6a). In the case of MDA-MB-231/MDA-MB-157 mixed aggregates, the application of blebbistatin was all that was required to reverse the sorting order of the cell lines (Figure 6b). This is in line with the high degree of disruption observed in monoculture MDA-MB-157 aggregates compared with that in MCF-10A cells under contractility inhibition, as well as the extremely potent effect of blebbistatin on MDA-MB-157 cells in contraction assays (Figure 4). Not only is blebbistatin effective in obtaining flipped organization during spheroid formation (starting from a mixture of dispersed, individual cells), but this method can also dynamically alter the organization of preexisting spheroids. Here, MDA-MB-231/MDA-MB-157 spheroids were formed with BME. Rather than resulting in partial sorting as in the case with no supplementation, this resulted in full sorting, with the MDA-MB-157 cells compactly in the interior of the mixed aggregate (Figure 6b). Such spheroids, when treated with blebbistatin, demonstrated dynamic inversion of the spatial organization over several days (Figure 6c; Supplemental Video S3). This simple method of inverting sorting demonstrates that knowledge of compaction behavior of cell lines in isolation informs sorting in coculture aggregates and provides a facile method for creating aggregates of controlled composition and organization. Furthermore, the treatment with contractility-modifying drugs is fast and completely reversible, so that once the desired coculture aggregate organization is achieved, the treatments can be washed out and the spheroids can be used in further assays (Supplemental Figure S12).

Collagen I spheroid invasion assays were then conducted with MDA-MB-231/MDA-MB-157 cocultured spheroids prepared with the distinct organizations induced by BME and blebbistatin. Such spheroids clearly demonstrated different invasion patterns. For BME-formed MDA-MB-231/MDA-MB-157 spheroids, with MDA-MB-231 cells on the outside of the spheroid, MDA-MB-231 cells invaded efficiently into the gel, displaying stellate morphology and invading in an individual migratory mode. MDA-MB-157 cells invaded poorly, with only a small number of individual cells seen at a distance from the spheroid core. However, even this limited invasion is greater than that seen in monoculture invasion assays of MDA-MB-157 (Supplemental Figure S1). Upon reversing the organization of the spheroid, MDA-MB-231 cell invasion was attenuated, ostensibly because the cells must navigate through the outer shell of MDA-MB-157 cells before invasion (Figure 6, d and e). Not only is MDA-MB-231 cell invasion attenuated by the presence of the MDA-MB-157 cells at the periphery of the spheroid, but a shift from individual invasion to a mixed individual and collective invasion was seen. This behavior is similar to one reported previously for cells prepared in a spheroid encased in a shell composed of BME (Guzman *et al.*, 2017) and one of presumed physiological relevance (Haeger *et al.*, 2015). As the MDA-MB-231 cells initially confined to the spheroid core invade into the surrounding collagen, they apparently facilitate invasion of the MDA-MB-157 cells further than they invade either in monoculture or when initially positioned in the coculture spheroid core. While the mechanisms by which this invasion facilitation occurs have not been characterized here, it is apparent that in coculture spheroids there are reciprocal interactions between cell lines that differ as a function of the spatial organization of the spheroid.

To demonstrate similar control over cell sorting and perturbation of cell invasive behavior in cells of the same genetic lineage, as would be expected to be present in tumors with distinct clonal populations, spheroids composed of MCF-10A and MCF-10AHRas cells were also investigated. MCF-10AHRas cells were created through transformation of MCF-10A cells with the oncogene Harvey rat sarcoma virus GTPase (HRas). HRas transformation triggers classical EMT changes in MCF-10A, including the loss of E-cadherin and an increase in N-cadherin and vimentin expression (Yoh *et al.*, 2016). MCF-10AHRas cells displayed significantly higher cellular contractility compared with MCF-10A cells and were invasive in 3D culture in collagen I, displaying individual invasion from spheroids similar to that of the other invasive cell types investigated in this work (Supplemental Figure S13, a and b). As expected given the previously determined sorting hierarchy, the diminished adhesivity in these cells driven primarily by the loss of E-cadherin caused MCF-10AHRas aggregates to be looser and more irregular in shape than MCF-10A aggregates, which is reflected in their characteristic compaction times (Supplemental Figure S13c). For poorly adhesive cell types, blebbistatin treatment has a beneficial effect on spheroid formation and this was indeed seen for MCF-10HRas spheroids (Supplemental Figure S13d). In mixed MCF-10A and MCF-10AHRas aggregates, full sorting occurred with MCF-10A cells at the spheroid core. Treatment with 5 μM blebbistatin did not lead to a full flip as in the MDA-MB-231/MDA-MB-157 combination but did result in the positioning of a significant portion of MCF-10AHRas cells in the interior of the spheroid (Supplemental Figure S13, e–g). Despite the fact that complete sorting inversion did not occur in these coculture spheroids, significant alterations in the invasive pattern as a function of initial spheroid organization were evident. Untreated spheroids, with MCF-10A cells situated entirely in the core and MCF-10AHRas cells on the periphery, showed a significant dispersal of MCF-10HRas cells, as well as the formation of a dense invasive front of individually invading MCF-10AHRas cells (Figure 6f). This invasive front promoted invasion of MCF-10A cells in collective multicellular streams as also reported previously (Carey *et al.*, 2013), a behavior that was not seen in spheroids composed solely of MCF-10A cells (Supplemental Figure S1). In contrast, spheroids prepared in the presence of blebbistatin showed much less invasion overall, with particular restraint of the otherwise highly invasive MCF-10AHRas cells (Supplemental Figure S6f). The dense invasive front of MCF-10AHRas cells was replaced by more sparsely invading individual cells. Most notably, the lack of a leading invasive front of MCF-10AHRas abolished the coinvasive behavior of MCF-10A cells, instead leading to noninvasive spreading also seen in monoculture MCF-10A (Supplemental Figure S1). In higher concentration collagen gels, a more dramatic difference was observed in the density of invading MCF-10HRas cells between spheroids with these cells positioned on the outside versus inside due to the denser, smaller-pore-size environment that provides physical challenges to invasion (Supplemental Figure S14) (Guzman *et al.*, 2014).

## DISCUSSION

The analysis of sorting behaviors in breast cell lines presented here demonstrates that consideration of adhesion proteins in combination with the principles of the differential adhesion hypothesis are

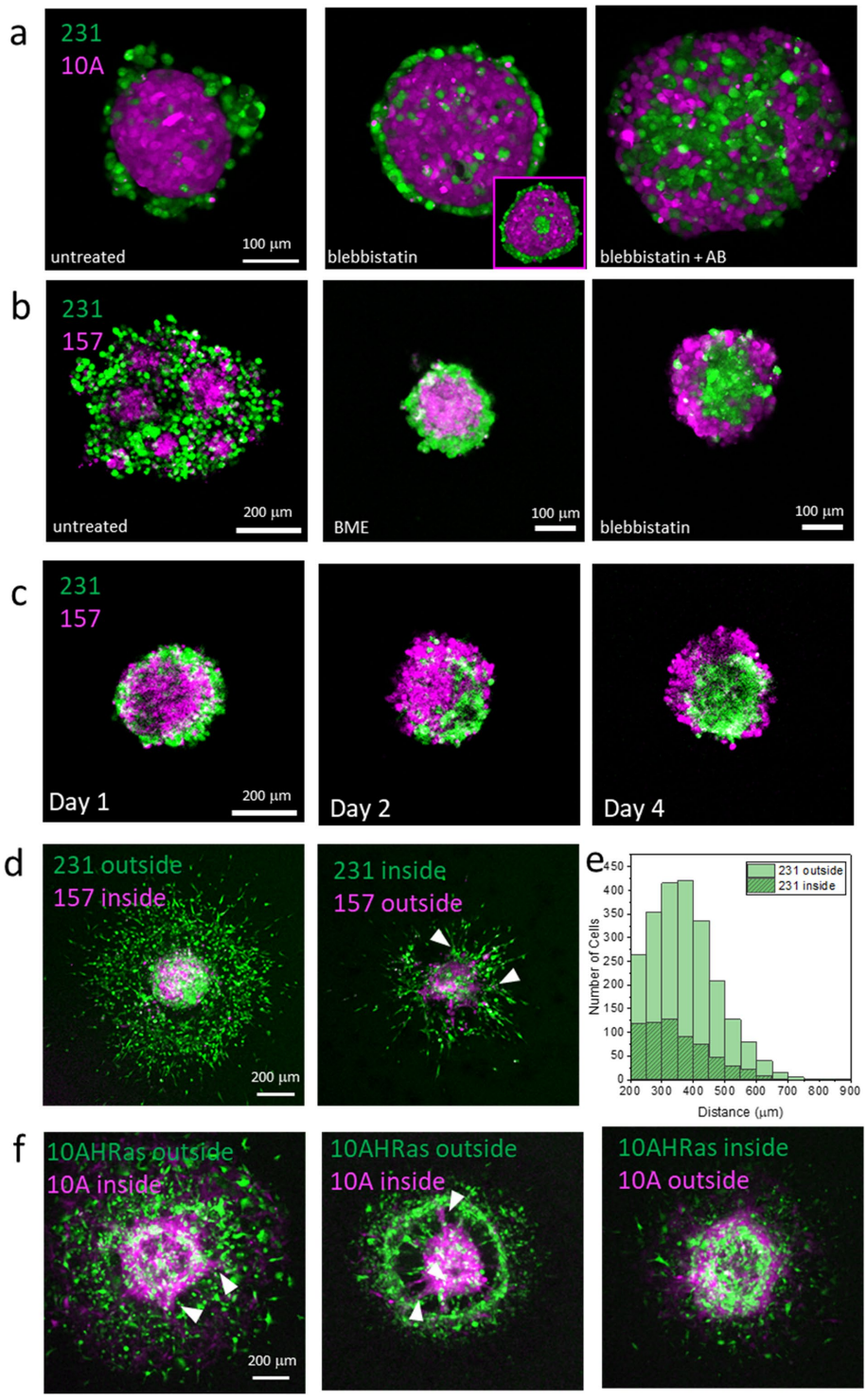


**FIGURE 6:** (a) MDA-MB-231 (green) and MCF-10A (magenta) mixed aggregates that are (from left to right) untreated, treated with 3.5 μM blebbistatin (inset, treated with 10 μM Y-27632), and treated with 3.5 μM blebbistatin and 10 μg/ml E-cadherin inhibitory antibody. Scale bar = 100 μm. (b) MDA-MB-231 (green) and MDA-MB-157 (magenta) aggregates that are (from left to right) untreated, supplemented with 0.2575 mg/ml BME, and treated with 5 μM blebbistatin. Scale bar (leftmost) = 200 μm; scale bar (middle and right) = 100 μm. (c) MDA-MB-231 (green) and MDA-MB-157 (magenta) aggregate formed with BME sorts such that MDA-MB-231 is located on the outside. Following treatment with Cell Recovery Solution (Corning) to remove BME and treatment with 5 μM blebbistatin, a sorting flip occurs. Images (from left to right) show the progressive change in organization at 0, 24, and 72 h after the beginning of blebbistatin treatment. (d) Invasion of a (left) BME-formed and (right) 5 μM blebbistatin-formed aggregate of MDA-MB-231 (green) and MDA-MB-157 (magenta) cells after 24 h invasion in a 1 mg/ml collagen I gel. White arrowheads indicate regions with collectively invading MDA-MB-231 cells. Scale bar (leftmost) = 200 μm. (e) Histogram of distances traveled by invading MDA-MB-231 cells from each spheroid formation condition. $n = 5$ spheroids for BME-formed spheroids (1724 cells) and $n = 7$ spheroids for blebbistatin-formed spheroids (791 cells). (f) (Left, middle cells) Invasion of an untreated aggregate of MCF-10AHRas (green) and MCF-10A (magenta) in a 1 mg/ml collagen I gel 24 h postimplantation. Image at the left is a maximum-intensity z-projection, and image in the middle is a select z-projection of the top portion of the spheroid. Collective invasion of MCF-10A cells is highlighted by white arrowheads. (Right) Invasion of an aggregate of MCF-10AHRas (green) and MCF-10A (magenta) cells treated with 5 μM blebbistatin in a 1 mg/ml collagen I gel 24 h postimplantation. Scale bar is 200 μm and the same in all panels.

useful as a minimal model with which to rationalize cancer cell sorting across the EMT. We find that cells with high invasive capacity tend to sort toward the outside of aggregates. This is due to a combination of factors associated with proinvasive behavior, primarily the loss of E-cadherin expression and the increase in actomyosin contractility. The general preference of more-invasive cell lines for the outside of aggregates may have implications for tumor invasion, as a small population of invasive cells in close proximity to the stromal environment may not only readily invade the surroundings but also reorganize the environment to be more permissive for other cells that may engage in leader-follower–type behavior (Gaggioli *et al.*, 2007; Carey *et al.*, 2013). This may in turn allow otherwise poorly invasive tumor cells to invade and adopt additional aberrant behaviors, as the extrusion of inherently less-invasive cells into the stromal compartment has the potential to trigger a switch to a more-invasive phenotype (Carey *et al.*, 2017).

In this work, we have demonstrated the importance of the interplay between cell adhesion and cortical tension in setting and controlling cell sorting behavior. We find that the primary adhesion proteins during the initial aggregation phase strongly dictate which cell line sorts to the inside of a mixed cell-type aggregate. Cells expressing high levels of cadherins are capable of forming cell–cell contacts rapidly, after which spheroids compact further through active contractility. For cell–cell adhesions mediated by integrins, a longer timescale is required for cells to be mechanically coupled.

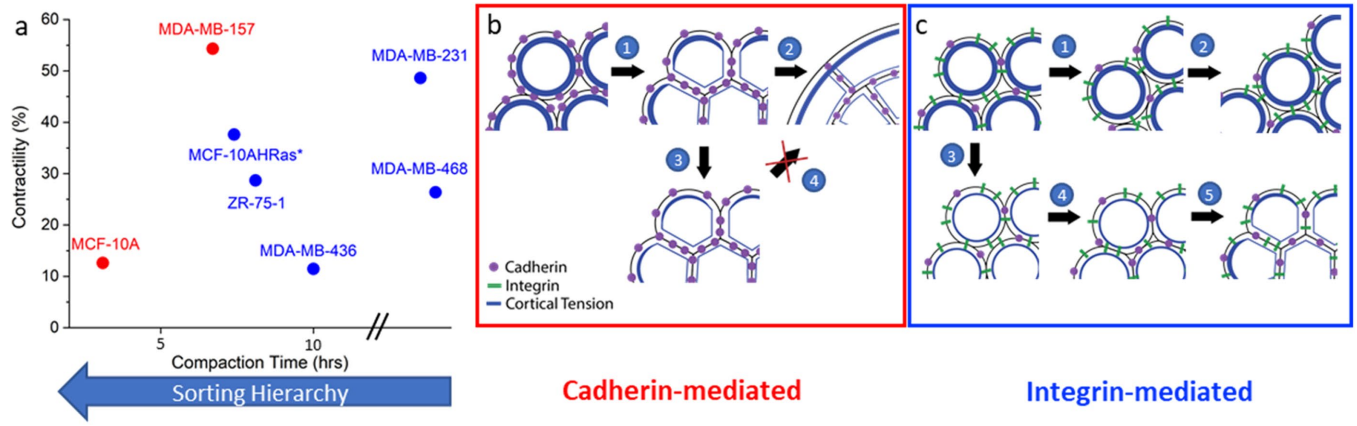


FIGURE 7: (a) Summary of cell lines investigated in this study with contractility as assessed through collagen contraction assays (shown also in Figure 4a, blue bars) plotted vs. compaction time of cells as single-cell-type spheroids (shown also in Figure 2d). Compaction of MDA-MB-231 and MDA-MB-468 cells cannot be quantified, but we place them on this plot to indicate slow compaction, with MDA-MB-231 cells placed to the left of MDA-MB-468 cells to reflect their relative tendency to compact to a certain degree over time (Supplemental Figure S6, a and b). Compaction time alone predicts sorting order in aggregates composed of pairs of cell lines. Cell lines labeled in red exhibit cadherin-mediated spheroid formation and are disrupted when contractility is reduced; cell lines labeled in blue exhibit integrin-mediated spheroid formation, and compaction is enhanced when contractility is reduced (Figure 4b). MCF-10AHRas cells are included in the graph with as asterisk, as their placement in the sorting hierarchy was not confirmed. (b, c) Schematic depiction of spheroid formation in two classes of spheroid formers. (b) In cadherin-mediated spheroid formation (cell lines labeled in red in a), cells rapidly form intercellular cadherin bonds (1). This leads to mechanical coupling between cells that allows reduction in tension at cell–cell interfaces, expansion of cell–cell contact areas, and redistribution of tension toward the aggregate edge. This results in mechanical polarization and eventual stretching of surface cells (2). Treatment with contractility inhibitors prevents cell stretching, but sufficient contractility generally remains for spheroid formation (3 and 4). (c) In an integrin-mediated compaction process (cell lines labeled in blue in a), significantly fewer cadherins are available for cell–cell adhesion; thus, integrins play a role. Adhesions in this case are transient, and cells pull apart and rearrange over time (1 and 2). Upon reduction of contractility, reduced cortex tension allows for more stable adhesions to develop, with sparse cadherins accumulating and integrins linking cells through ECM. Over time, cell–cell contact areas expand as facilitated by the reduced cortex tension, and a more cohesive spheroid forms (3–5).

This may be due to the low concentration of ECM molecules for adhesion in media, slow accumulation of cadherins in initial loose aggregates, or a combination of these factors.

Among the cell lines investigated here, we have identified a unique role for actomyosin contractility among cells that compact via slow (integrin based) and fast (cadherin based) compaction (schematically depicted in Figure 7). Rapidly compacting cell lines (Figure 7, a, red points, and b), such as MCF-10A, tend to form aggregates with characteristic stretched surface cells that are associated with mechanical polarization of tissue from coregulation of adhesion and cortical tension. During spheroid formation, the stretching of surface cells indicates that these cells are in a regime where cortical tension is higher at cell–media interfaces than cell–cell interfaces (Manning *et al.*, 2010). Decreasing contractility disrupts this process and leads to surface cell rounding and spheroid disruption. The response of cadherin-mediated spheroid formers to decreasing cellular contractility is consistent with previous models for cell adhesion in confluent monolayers and 3D aggregates (Manning *et al.*, 2010). When contractility is properly regulated with mechanically coupled cells, it is advantageous for spheroid formation.

For cell lines that compact using integrin-mediated processes (Figure 7, a, blue points, and c), cadherin deficiency shapes and slows the aggregation process. High levels of contractility become disadvantageous for spheroid formation. Cortical tension present in highly contractile cells lacking cadherins inhibits formation of stable cell–cell contacts, as loosely attached cells round up and pull away from one another. Such contractility serves as an effective repulsion between cells (Supplemental Video S2). Here, reducing cellular contractility can push cells to a regime where robust spheroid formation can occur. While most of the inhibitory pharmacological treatments explored in this work have a favorable effect on spheroid formation for cell types lacking cadherins, in cases where particularly high concentrations could be achieved and were investigated, aggregate cohesion plateaued and ultimately diminished, as would be expected in cases where contractility is too low or absent (Supplemental Figure S10). While decreasing contractility is not generally understood to enhance aggregation, this finding is consistent with the previous finding that high cortex tension in microtissues of constrained geometries can lead to tissue failure (Dean and Morgan, 2008; Wang *et al.*, 2013).

It has been shown in other work that actomyosin contractility is generally advantageous for forming tight aggregates, with cells possessing higher levels of contractility demonstrating preference for the inside of aggregates in germ layer sorting (Krieg *et al.*, 2008). Instrumental in this hypothesis is the fact that cells can redistribute tension throughout the forming aggregate so that high cortical tension between cells does not hamper adhesion as tissue boundaries are established (Amack and Manning, 2012). Here, a critical step is the mechanical coupling of cells through cadherin–cytoskeletal linkages mediated by adapter proteins, which allow for tension redistribution to occur (Maître *et al.*, 2012). Investigations of cell–cell contacts in two-dimensional culture have demonstrated Rho signaling downstream of cadherin bond formation that allows full expansion of the cell–cell contact to maximize adhesion while maintaining high tension toward the cell–media interfaces (Yamada and Nelson, 2007).

Actomyosin contractility drives contact expansion while not hampering cell adhesion formation by pulling cells apart from one another. Even in cells that are well-coupled through cadherin-based adhesions, there is evidence that the contractile nature of cells can hinder cell–cell adhesion. ROCK activation has been shown to disrupt adherens junctions in Madin–Darby canine kidney monolayers, and myosin II activity can unzip cell contacts if actin dynamics are not precisely regulated (Sahai and Marshall, 2002; He Li *et al.*, 2020). These results highlight the dynamic nature of adhesions and the perhaps underappreciated instability that can arise under forces typical of epithelial cell adhesion. In the cell types investigated here that undergo cadherin-mediated compaction, mechanical coupling allows efficient compaction in both high- and low-contractility regimes. In contrast, for cells that undergo integrin-driven compaction, which are typically far along in the EMT and lacking in E-cadherins, the cells are not initially stably mechanically coupled in the same way that is achieved through cadherin–cadherin bonds. In this case, high cell contractility acts as an effective repulsion, pulling cells away from one another. Low-adhesion, high-contractility cell types thus experience a dramatic compaction enhancement with contractility inhibition. In spheroids in which one cell type exhibits cadherin-driven compaction and the other exhibits integrin-driven compaction, treatment with a contractility inhibitor can be expected to significantly alter cell positioning in an aggregate, favoring less-aggressive cells at the periphery and more-aggressive ones in the core of the aggregate.

The restoration of cell–cell contacts in poorly adhesive, transformed cell types upon contractility inhibition may represent a shift back toward a more epithelial phenotype (Zhong *et al.*, 1997). As discussed previously, high contractility is a feature of EMT progression that is associated with aggressive invasion and matrix remodeling (Samuel *et al.*, 2011). However, contractility that is beneficial for initial invasion may discourage cell survival in the collagen-rich stroma, where lack of cell–cell contacts triggers apoptotic pathways (Schipper *et al.*, 2019; Yu, 2019). E-cadherin–deficient invading cells in a mouse model show enhanced survival when cultured with blebbistatin. In that work, once cells invaded the collagen-rich stroma, reduction in contractility allowed not only enhanced survival but also secondary tumor formation. This could be a mechanism through which tumor cells cycle between an aggressive invasive phenotype and a proliferative, tumor-initiating phenotype. Additionally, this result may shed light on the underlying mechanism of the beneficial effects of the ROCK inhibitor Y-27632 in cell culture, which has long been used as a supplement in primary cell culture, specifically in breast cancer organoids (Liu *et al.*, 2012; Sachs *et al.*, 2018).

The fact that simple actomyosin contractility inhibition can encourage significantly more-robust cell–cell contacts can have multiple applications. First, reduction of actomyosin contractility serves as a useful strategy for spheroid formation in cell lines in which it is otherwise difficult to do so, such as MDA-MB-468 cells. Second, minitissues or other complex in vitro cell assemblies could be made using insights gleaned from the work described here. Third, the ability to control cell sorting using methods described here can serve as a potential strategy to limit invasion through encouraging compaction and relocation of invasive cell types in aggregates. While other methods exist to achieve controlled aggregates or organization of mixed cell types, they typically involve complex genetic alterations that are time intensive to implement (Toda *et al.*, 2018). Containment of such cells in the interior of an aggregate prevents easy access to the stromal compartment and subsequent coinvasion with other subpopulations of cells. The strategy may be especially impactful, as it exploits the differential effect of contractility modification on generally invasive versus noninvasive cells and thus requires only a single treatment to target both cell populations with the outcome of creating a physical barrier to invasion, potentially not only in in vitro environments such as spheroids or organoids but also in vivo.

## MATERIALS AND METHODS

Request a protocol through *Bio-protocol*.

### Cell lines and reagents

For detailed cell line and reagent listings, see the Supplemental Information.

### Cell culture

Cell culture was performed via established methods. For detailed protocols, see the Supplemental Information.

### Gel contraction and collagen invasion assays

Gel contraction and collagen invasion assays were performed as described previously in Ziperstein *et al.* (2015). For a more-detailed description, see the Supplemental Information.

### Microscopy

Laser-scanning confocal microscopy was used for fixed sample imaging. Laser-scanning confocal and widefield microscopy were used for live sample imaging. Full details of imaging conditions are in the Supplemental Information.

### Sorting experiments

Before being mixed, cells were labeled with fluorescent cytosolic dyes, Cell Tracker Green CMFDA and Cell Tracker Orange CMRA (Invitrogen), according to the manufacturer's protocol. Cells were incubated with the staining solution (2 µM CMFDA and 7 µM CMRA) in serum-free medium for 45 min at 37°C and were washed twice with phosphate-buffered saline before detachment via Accutase. Cells were counted and mixed in a 1:1 ratio. For cell lines using different media, cell suspensions were mixed such that the different media were mixed at a 1:1 ratio as well. Cell mixtures were plated in an ultra-low-attachment 96-well plate such that each well contained a total of 2000 cells, and the plate was then centrifuged at 1000 × *g* for 10 min at 4°C. The plate was transferred to a 37°C incubator with 5% $CO_2$. The plate was removed from the incubator for imaging with a 10× air objective on a confocal laser-scanning microscope (Olympus Fluoview 300) at 2, 24, 48, and 72 h time points following centrifugation. To capture the entire spheroid during formation, 100 µm stacks with 5 µm steps were collected. Fluorescence imaging was performed using 488 and 543 nm lasers, and fluorescence was detected on photomultiplier tube detectors.

### Image analysis

Image analyses were performed using ImageJ, Python, and Matlab. Analysis of cell sorting was performed as described in Cochet-Escartin *et al.* (2017). For full details regarding analysis of sorting dynamics and other image analyses, see the Supplemental Information.

### Spheroid compaction and inhibitory treatments

Spheroid experiments were performed by plating cells in ultra-low-adhesion plates and centrifuging. Transmitted light images were taken periodically to monitor aggregation. Media supplementation was performed during the formation period to either encourage or inhibit spheroid formation. For details on supplements, concentrations, and quantification, see the Supplemental Information.

### siRNA-mediated $\beta_1$ integrin knockdown

siRNA knockout was performed using standard lipid-mediated transfection methods. For a detailed protocol and quantification of efficiency, see the Supplemental Information.

### Immunocytochemistry

Cell fixation and immunofluorescence were performed using established methods. For full details, see the Supplemental Information.

### Statistical analysis

Statistical analyses for each data set were performed using R. Details are given in the figure captions and the Supplemental Information.

### Data sharing

All study data are included in the article or the Supplemental Information. Raw data are available upon request.

## ACKNOWLEDGMENTS

A.J.D. was supported in part through Columbia University's NIH Training Program in Molecular Biophysics (T32-GM008281). M.B.V. was supported in part through the Beckman Scholars Program. Live cell imaging on the Cytation 5 in this work was performed in the Confocal and Specialized Microscopy Shared Resource of the Herbert Irving Comprehensive Cancer Center at Columbia University, supported by National Institutes of Health Grant #P30 CA013696 (National Cancer Institute). We thank Lucas Kampmann and Joseph Hammer for assistance with live cell imaging.

## REFERENCES

Amack JD, Manning ML (2012). Knowing the boundaries: extending the differential adhesion hypothesis in embryonic cell sorting. Science 338, 212–215.

Atia L, Bi D, Sharma Y, Mitchel JA, Gweon B, Koehler SA, Decamp SJ, Lan B, Kim JH, Hirsch R, *et al.* (2018). Geometric constraints during epithelial jamming. Nat Phys 14, 613–620.

Bécam I, Huynh JR (2007). Genetic control of intercellular adhesion or how cadherins shape the fruitfly Drosophila melanogaster. Med Sci (Paris) 3, 285–290.

Beysens DA, Forgacs G, Glazier JA (2000). Cell sorting is analogous to phase ordering in fluids. Proc Natl Acad Sci USA 97, 9467–9471.

Bi D, Yang X, Marchetti MC, Manning ML (2016). Motility-driven glass and jamming transitions in biological tissues. Phys Rev X 6, 021011.

Blick T, Widodo E, Hugo H, Waltham M, Lenburg ME, Neve RM, Thompson EW (2008). Epithelial mesenchymal transition traits in human breast cancer cell lines. Clin Exp Metastasis 25, 629–642.

Carey SP, Martin KE, Reinhart-King CA (2017). Three-dimensional collagen matrix induces a mechanosensitive invasive epithelial phenotype. Sci Rep 7, 42088.

Carey SP, Starchenko A, McGregor AL, Reinhart-King CA (2013). Leading malignant cells initiate collective epithelial cell invasion in a three-dimensional heterotypic tumor spheroid model. Clin Exp Metastasis 30, 615–630.

Chavez KJ, Garimella SV, Lipkowitz S (2010). Triple negative breast cancer cell lines: one tool in the search for better treatment of triple negative breast cancer. Breast Dis 32, 35–48.

Cochet-Escartin O, Locke TT, Shi WH, Steele RE, Collins EMS (2017). Physical mechanisms driving cell sorting in hydra. Biophys J 113, 2827–2841.

Dahmann C, Oates AC, Brand M (2011). Boundary formation and maintenance in tissue development. Nat Rev Genet 12, 43–55.

Dean DM, Morgan JR (2008). Cytoskeletal-mediated tension modulates the directed self-assembly of microtissues. Tissue Eng Part A 14, 1989–1997.

Fan X, Diamond PH, Chacón L, Li H (2016). Cascades and spectra of a turbulent spinodal decomposition in two-dimensional symmetric binary liquid mixtures. Phys Rev Fluids 1, 054403.

Foty RA, Pfleger CM, Forgacs G, Steinberg MS (1996). Surface tensions of embryonic tissues predict their mutual envelopment behavior. Development 122, 1611–1620.

Foty RA, Steinberg MS (2004). Cadherin-mediated cell-cell adhesion and tissue segregation in relation to malignancy. Int J Dev Biol 48, 397–409.

Foty RA, Steinberg MS (2005). The differential adhesion hypothesis: a direct evaluation. Dev Biol 278, 255–263.

Froehlich K, Haeger J-D, Heger J, Pastuschek J, Photini SM, Yan Y, Lupp A, Pfarrer C, Mrowka R, Schleußner E, *et al.* (2016). Generation of multicellular breast cancer tumor spheroids: comparison of different protocols. J Mammary Gland Biol Neoplasia 21, 89–98.

Gaggioli C, Hooper S, Hidalgo-Carcedo C, Grosse R, Marshall JF, Harrington K, Sahai E (2007). Fibroblast-led collective invasion of carcinoma cells with differing roles for RhoGTPases in leading and following cells. Nat Cell Biol 9, 1392–1400.

Gamboa Castro M, Leggett SE, Wong IY (2016). Clustering and jamming in epithelial-mesenchymal co-cultures. Soft Matter 12, 8327–8337.

Garcia-Bellido A, Ripoll P, Morata G (1973). Developmental compartmentalisation of the wing disk of drosophila. Nat New Biol 245, 251–253.

Guzman A, Sánchez Alemany V, Nguyen Y, Zhang CR, Kaufman LJ (2017). A novel 3D in vitro metastasis model elucidates differential invasive strategies during and after breaching basement membrane. Biomaterials 115, 19–29.

Guzman A, Ziperstein MJ, Kaufman LJ (2014). The effect of fibrillar matrix architecture on tumor cell invasion of physically challenging environments. Biomaterials 35, 6954–6963.

Haeger A, Wolf K, Zegers MM, Friedl P (2015). Collective cell migration: guidance principles and hierarchies. Trends Cell Biol 25, 556–566.

Harris AK (1976). Is cell sorting caused by differences in the work of intercellular adhesion? A critique of the Steinberg hypothesis. J Theor Biol 61, 267–285.

He Li JX, Tang VW, Brieher WM (2020). Actin protrusions push at apical junctions to maintain E-cadherin adhesion. Proc Natl Acad Sci USA 117, 432–438.

Ivascu A, Kubbies M (2006). Rapid generation of single-tumor spheroids for high-throughput cell function and toxicity analysis. J Biomol Screen 11, 922–932.

Ivascu A, Kubbies M (2007). Diversity of cell-mediated adhesions in breast cancer spheroids. Int J Oncol 31, 1403–1413.

Kao J, Salari K, Bocanegra M, Choi Y-L, Girard L, Gandhi J, Kwei KA, Hernandez-Boussard T, Wang P, Gazdar AF, et al. (2009). Molecular profiling of breast cancer cell lines defines relevant tumor models and provides a resource for cancer gene discovery. PLoS One 4, e6146.

Kenny PA, Lee GY, Myers CA, Neve RM, Semeiks JR, Spellman PT, Lorenz K, Lee EH, Barcellos-Hoff MH, Petersen OW, *et al.* (2007). The morphologies of breast cancer cell lines in three-dimensional assays correlate with their profiles of gene expression. Mol Oncol 1, 84–96.

Képiró M, Várkuti BH, Végner L, Vörös G, Hegyi G, Varga M, Málnási-Csizmadia A (2014). Para-nitroblebbistatin, the non-cytotoxic and photostable myosin II inhibitor. Angew Chem Int Ed Engl 126, 8350–8354.

Krieg M, Arboleda-Estudillo Y, Puech PH, Käfer J, Graner F, Müller DJ, Heisenberg CP (2008). Tensile forces govern germ-layer organization in zebrafish. Nat Cell Biol 10, 429–436.

Labernadie A, Kato T, Brugués A, Serra-Picamal X, Derzsi S, Arwert E, Weston A, González-Tarragó V, Elosegui-Artola A, Albertazzi L, *et al.* (2017). A mechanically active heterotypic E-cadherin/N-cadherin adhesion enables fibroblasts to drive cancer cell invasion. Nat Cell Biol 19, 224–237.

Lehmann BD, Bauer JA, Chen X, Sanders ME, Chakravarthy AB, Shyr Y, Pietenpol JA (2011). Identification of human triple-negative breast cancer subtypes and preclinical models for selection of targeted therapies. J Clin Invest 121, 2750–2767.

Li J, Su Y, Xia W, Qin Y, Humphries MJ, Vestweber D, Cabañas C, Lu C, Springer TA (2017). Conformational equilibria and intrinsic affinities define integrin activation. EMBO J 36, 629–645.

Lin RZ, Chou LF, Chien CCM, Chang HY (2006). Dynamic analysis of hepatoma spheroid formation: roles of E-cadherin and β1-integrin. Cell Tissue Res 324, 411–422.

Liu X, Ory V, Chapman S, Yuan H, Albanese C, Kallakury B, Timofeeva OA, Nealon C, Dakic A, Simic V, *et al.* (2012). ROCK inhibitor and feeder cells induce the conditional reprogramming of epithelial cells. Am J Pathol 180, 599–607.

Maître JL, Berthoumieux H, Krens SFG, Salbreux G, Jülicher F, Paluch E, Heisenberg CP (2012). Adhesion functions in cell sorting by mechanically coupling the cortices of adhering cells. Science 338, 253–256.

Malinverno C, Corallino S, Giavazzi F, Bergert M, Li Q, Leoni M, Disanza A, Frittoli E, Oldani A, Martini E, *et al.* (2017). Endocytic reawakening of motility in jammed epithelia. Nat Mater 16, 587–596.

Manning ML, Foty RA, Steinberg MS, Schoetz EM (2010). Coaction of intercellular adhesion and cortical tension specifies tissue surface tension. Proc Natl Acad Sci USA 107, 12517–12522.
Oswald L, Grosser S, Smith DM, Käs JA (2017). Jamming transitions in cancer. J Phys D Appl Phys 50, 483001.
Palamidessi A, Malinverno C, Frittoli E, Corallino S, Barbieri E, Sigismund S, Beznoussenko GV, Martini E, Garre M, Ferrara I, *et al.* (2019). Unjamming overcomes kinetic and proliferation arrest in terminally differentiated cells and promotes collective motility of carcinoma. Nat Mater 18, 1252–1263.
Pastushenko I, Blanpain C (2019). EMT transition states during tumor progression and metastasis. Trends Cell Biol 29, 212–226.
Pawlizak S, Fritsch AW, Grosser S, Ahrens D, Thalheim T, Riedel S, Kießling TR, Oswald L, Zink M, Manning ML, *et al.* (2015). Testing the differential adhesion hypothesis across the epithelial-mesenchymal transition. New J Phys 17, 083049.
Robinson EE, Foty RA, Corbett SA (2004). Fibronectin matrix assembly regulates α5β1-mediated cell cohesion. Mol Biol Cell 15, 973–981.
Sachs N, de Ligt J, Kopper O, Gogola E, Bounova G, Weeber F, Balgobind AV, Wind K, Gracanin A, Begthel H, *et al.* (2018). A living biobank of breast cancer organoids captures disease heterogeneity. Cell 172, 373–386.
Sahai E (2005). Mechanisms of cancer cell invasion. Curr Opin Genet Dev 15, 87–96.
Sahai E, Marshall CJ (2002). ROCK and Dia have opposing effects on adherens junctions downstream of Rho. Nat Cell Biol 4, 408–415.
Samuel MS, Lopez JI, McGhee EJ, Croft DR, Strachan D, Timpson P, Munro J, Schröder E, Zhou J, Brunton VG, *et al.* (2011). Actomyosin-mediated cellular tension drives increased tissue stiffness and β-catenin activation to induce epidermal hyperplasia and tumor growth. Cancer Cell 19, 776–791.
Schipper K, Seinstra D, Paulien Drenth A, van der Burg E, Ramovs V, Sonnenberg A, van Rheenen J, Nethe M, Jonkers J (2019). Rebalancing of actomyosin contractility enables mammary tumor formation upon loss of E-cadherin. Nat Commun 10, 3800.
Steinberg MS (1962). On the mechanism of tissue reconstruction by dissociated cells. I. Population kinetics, differential adhesiveness. and the absence of directed migration. Proc Natl Acad Sci USA 48, 1577–1582.
Steinberg MS (1963). Reconstruction of tissues by dissociated cells. Science 141, 401–408.
Steinberg MS (2007). Differential adhesion in morphogenesis: a modern view. Curr Opin Genet Dev 17, 281–286.
Subik K, Lee J-F, Baxter L, Strzepek T, Costello D, Crowley P, Xing L, Hung M-C, Bonfiglio T, Hicks DG, *et al.* (2010). The expression patterns of ER, PR, HER2, CK5/6, EGFR, Ki-67 and AR by immunohistochemical analysis in breast cancer cell lines. Breast Cancer (Auckl) 4, 35–41.
Technau U, Holstein TW (1992). Cell sorting during the regeneration of hydra from reaggregated cells. Dev Biol 151, 117–127.
Toda S, Blauch LR, Tang SKY, Morsut L, Lim WA (2018). Programming self-organizing multicellular structures with synthetic cell-cell signaling. Science 361, 156–162.
Uehata M, Ishizaki T, Satoh H, Ono T, Kawahara T, Morishita T, Tamakawa H, Yamagami K, Inui J, Maekawa M, *et al.* (1997). Calcium sensitization of smooth muscle mediated by a Rho-associated protein kinase in hypertension. Nature 389, 990–994.
Vant Veer LJ, Dai H, van de Vijver MJ, He YD, Hart AAM, Mao M, Peterse HL, van der Kooy K, Marton MJ, Witteveen AT, *et al.* (2002). Gene expression profiling predicts clinical outcome of breast cancer. Nature 415, 530–536.
Várkuti BH, Képiró M, Horváth IÁ, Végner L, Ráti S, Zsigmond Á, Hegyi G, Lenkei Z, Varga M, Málnási-Csizmadia A (2016). A highly soluble, non-phototoxic, non-fluorescent blebbistatin derivative. Sci Rep 6, 26141.
Wang H, Svoronos AA, Boudou T, Sakar MS, Schell JY, Morgan JR, Chen CS, Shenoy VB (2013). Necking and failure of constrained 3D microtissues induced by cellular tension. Proc Natl Acad Sci USA 110, 20923–20928.
Winklbauer R (2019). Dynamic cell-cell adhesion mediated by pericellular matrix interaction—a hypothesis. J Cell Sci 132, 1–10.
Yamada S, Nelson WJ (2007). Localized zones of Rho and Rac activities drive initiation and expansion of epithelial cell-cell adhesion. J Cell Biol 178, 517–527.
Yang X, Bi D, Czajkowski M, Merkel M, Manning ML, Marchetti MC (2017). Correlating cell shape and cellular stress in motile confluent tissues. Proc Natl Acad Sci USA 114, 12663–12668.
Yoh KE, Regunath K, Guzman A, Lee S-M, Pfister NT, Akanni O, Kaufman LJ, Prives C, Prywes R (2016). Repression of p63 and induction of EMT by mutant Ras in mammary epithelial cells. Proc Natl Acad Sci USA 113, E6107–E6116.
Yu M (2019). Metastasis stemming from circulating tumor cell clusters. Trends Cell Biol 29, 275–276.
Zhong C, Kinch MS, Burridge K (1997). Rho-stimulated contractility contributes to the fibroblastic phenotype of Ras-transformed epithelial cells. Mol Biol Cell 8, 2329–2344.
Ziperstein MJ, Guzman A, Kaufman LJ (2015). Breast cancer cell line aggregate morphology does not predict invasive capacity. PLoS One 10, e0139523.